

Shared Microexponents: A Little Shifting Goes a Long Way

Bitā Rouhani*, Ritchie Zhao, Venmugil Elango, Rasoul Shafipour, Mathew Hall, Maral Mesmakhosroshahi, Ankit More, Levi Melnick, Maximilian Golub, Girish Varatkar, Lei Shao, Gaurav Kolhe, Dimitry Melts, Jasmine Klar, Renee L’Heureux, Matt Perry, Doug Burger, Eric Chung

Microsoft

Zhaoxia Deng, Sam Naghshineh, Jongsoo Park, Maxim Naumov

Meta

Abstract—This paper introduces Block Data Representations (BDR), a framework for exploring and evaluating a wide spectrum of narrow-precision formats for deep learning. It enables comparison of popular quantization standards, and through BDR, new formats based on shared microexponents (MX) are identified, which outperform other state-of-the-art quantization approaches, including narrow-precision floating-point and block floating-point. MX utilizes multiple levels of quantization scaling with ultra-fine scaling factors based on shared microexponents in the hardware. The effectiveness of MX is demonstrated on real-world models including large-scale generative pretraining and inferencing, and production-scale recommendation systems.

I. INTRODUCTION

The disruptive AI capabilities that are rapidly emerging are driven primarily by scale. With each order-of-magnitude increase, models (particularly large language models such as GPT-3) show amazing and surprising capabilities emerging. Unfortunately, that same scale results in high computation and energy costs to train and serve these models.

The AI industry is applying many techniques to reduce the costs of models at each scale point. Quantization of tensor values is one important instance of these techniques, in which the individual tensor values are cast from FP32 to a cheaper numeric standard. Given the importance, there has been a marked increase in quantization formats, papers, and implementations over the past few years. Nvidia’s support for an FP8 standard is one important recent example [37].

Quantization standards aim to balance three factors that can trade off against one another:

- Efficiency, a combination of compute efficiency (energy and silicon area for dot products) and memory efficiency (the bits required to store or communicate a tensor).
- Accuracy (or “model performance” in AI parlance), the amount of loss (reduced quality of results) incurred by the quantization compared to FP32 precision.
- Friction, the user effort required to apply the quantization format effectively. Friction can arise from uneven results

across different model classes, or from the need to tweak software parameters to achieve the target accuracy.

Many competing data formats have been proposed, and the design space of possible new ideas is rich. The diversity of numeric formats makes for a complex space given subtle trade-offs between efficiency, accuracy, and friction. In this paper, we describe a framework that encompasses much of the quantization design space. This framework, which we call Block Data Representations (BDR) defines the ways to quantize and scale sets of tensor values collectively. Design points in this space may have large sets (e.g., $\sim 1K$) or small sets (e.g., ~ 10), they may use integer or floating-point scaling factors, the scaling factors may be applied by hardware or software, and there may be multiple levels of scaling among different sets of the values.

Using the BDR framework, we survey and evaluate many of the popular quantization standards, including INT4, INT8, variants of FP8 [37], VSQ [23], and block floating-point variants (including MSFP [24]). To evaluate quantization accuracy, we define a statistical methodology that computes quantization signal-to-noise ratio, validating it against a range of real models. To measure hardware efficiency, we define a dot product engine in a leading process node that enables the computation of synthesized power and area for different quantization configurations. Leveraging these two models, we sweep hundreds of configurations in the design space and construct a Pareto frontier of the best accuracy and efficiency quantization design points.

Finally, with the BDR framework, we describe a new numerical approach to quantization formats based on shared microexponents (MX). MX leverages multiple levels of quantization scaling, but unlike prior multi-level approaches such as FP8 and VSQ, it uses fine-grained scaling factors (~ 10 elements) and ultra-fine-grained level-two scaling factors (one bit exponent shared by two elements), both set in the hardware. The fine-grained scaling factor reduces the numerical blast radius from outliers, and the ultra-fine-grained second-level scaling factor provides additional noise reduction, with no software friction since all scaling factors are automatically set

*Corresponding Author. Email: bita.rouhani@microsoft.com

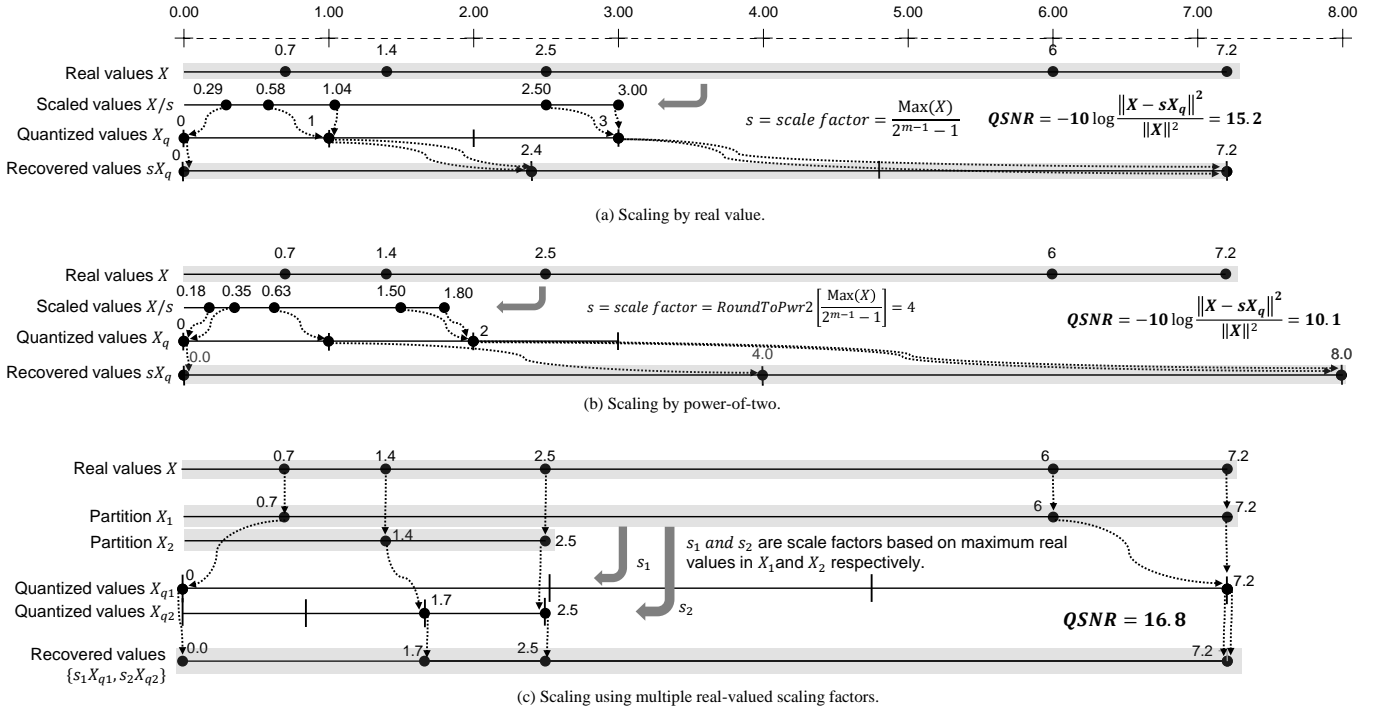


Fig. 1: (a) INT-based quantization with FP32-based scaling based on maximum value, (b) Scaling is constrained to powers of two for hardware efficiency, (c) Multiple scaling factors enable increased resolution and reduced quantization error.

by hardware.

The accuracy and efficiency models demonstrate that the MX approach creates a new Pareto frontier which makes many of its design points best in class compared to the other popular quantization approaches. We identify three members of the MX family (4, 6, and 9 bits, respectively) as being the most desirable to include as a set in silicon implementations. These three design points sit close to the new Pareto frontier. They provide a range of accuracy/efficiency/friction design points that align with the scenarios most commonly used by practitioners in both training and inference. Finally, they use a relatively small number of elements for the shared level-one scaling factor, making them easy to incorporate in a wide range of tensor unit designs and more amenable to fine-grained sparsity support than larger block sizes.

II. QUANTIZATION OVERVIEW

In deep learning, quantization refers to the process of numerically constraining a model’s set of weights, activations, and gradients to compact representations, e.g., from 32-bit floating-point values to 4-bit INTs. Quantization can be used to improve the efficiency of memory and communication, or to accelerate computations during both training and inferencing.

INT Quantization. Uniform INT-based quantization is a popular method that maps real values to INTs. As illustrated in Figure 1 (a), a set of real values X are mapped symmetrically and uniformly to INTs $X_q \in [-2^{m-1}, 2^{m-1} - 1]^k$ where m is the size of a two’s complement number and k is the number of values to be quantized together ($k = 5$ in the figure). A quantization scaling factor s is applied to the k

values such that they map into INTs after rounding ($X_q = \text{RoundToInt}(X/s)$). One method to compute a scaling factor is to align the maximum-observed value within the k values to the largest representable INT:

$$s = \frac{\text{Max}(X)}{2^{m-1} - 1}. \quad (1)$$

The overall quantization function is thus:

$$X_q = Q(X, s) = \text{RoundToInt}(X/s). \quad (2)$$

Performing the descaling step, sX_q , restores quantized values into the original scale.

Scaling Strategies. As illustrated in Figure 1 (a)-(b), there are various methods for encoding and computing with scale factors, including the use of more hardware-efficient quantized power-of-two or INT representations. The optimal scaling approach depends on factors such as implementation complexities and overheads, and has a first-order impact on quantization error (see QSNR definition in Section IV). Producing scaling factors for static values, such as pre-trained weights, is relatively straightforward. However, handling dynamic activations and gradients with data-dependent numerical distributions is more challenging. Thus it is necessary to employ strategies such as assigning conservative scaling factors to guard against dynamic outliers or utilizing dynamic scaling approaches that update the scaling factor as distributions change.

Coarse-grained Scaling Support in SW. Many software-based scaling strategies have been proposed in the literature, as surveyed in [31]. Partitioning an initial set of values into multiple sets and introducing multiple scaling factors, as shown

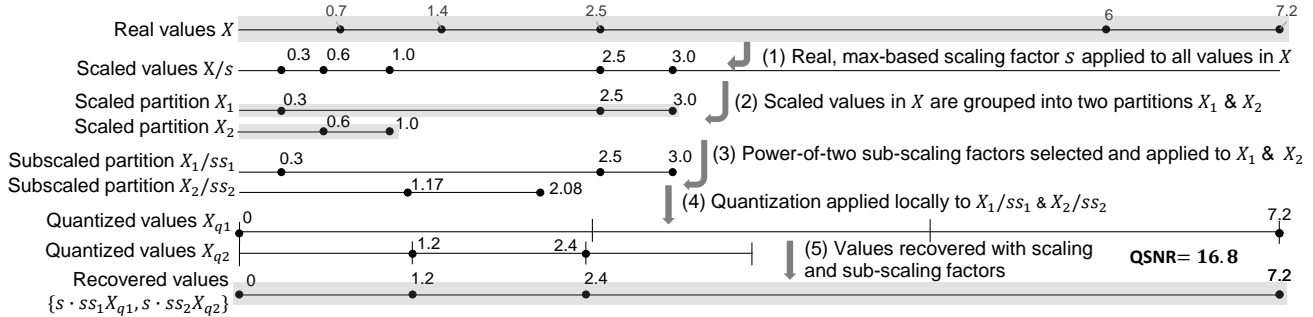


Fig. 2: Example of a two-level scaling approach approximating ideal FP32-based scaling on two partitions. Low-cost sub-scale factors encoded in powers of two are composed with a top-level FP32 scaling factor to finetune scaling within each partition.

in the example of Figure 1 (c), is an effective approach to mitigate outliers and reduce quantization error. Unfortunately, today’s software-based approaches are limited to coarse-grain scaling factors that must be amortized efficiently across a large number of values to be quantized (referred to as block granularity k throughout this paper) [47]. In practice, most software-based INT scaling methods in modern GPUs require $\sim 1K$ elements to balance efficiency and model accuracy. Larger values of k , coupled with the limitations of maintaining scaling factors at low overheads, also limit the opportunity to reduce quantization bit-width, which is needed to provide enough resolution to encode a large set of quantized values while minimizing quantization error.

Fine-grained Scaling Support in HW. Block Floating-Point (BFP)-inspired approaches such as MSFP [24] and Hybrid BFP [29] diminish the impact of outliers by introducing dedicated hardware support for fine-grained scaling on the order of $k \sim 10$ that reduces or eliminates the need for software-based heuristics. BFP is closely related to INT-based quantization based on the same principles, with the exception that the scaling factors are constrained to powers of two, which are practical to implement in hardware at a fine granularity (typically within a single dot product unit).

Figure 3 gives a visual intuition of quantization implemented with coarse-grained software versus fine-grained HW-based BFP. While both approaches operate on the same principles, the offloading of fine-grain scaling into HW enables much higher effective resolution in BFP vs. INT.

III. MULTI-LEVEL SCALING

In this section, we extend the characterization of the aforementioned quantization and scaling approaches to newer techniques such as FP8, under the umbrella framework of BDR. As implied in Section II, various hardware/software quantization approaches must balance block granularity (k) and the complexity and cost of handling scale factors. Given a finite number of bits, the objective is to construct a high-fidelity representation that minimizes computational and memory overheads and closely approximates full-precision scaling factors. In general, we expect quantization error to decrease with smaller k granularity and increased precision of scaling factors (e.g., FP32 vs. power-of-two). Decreasing k and/or

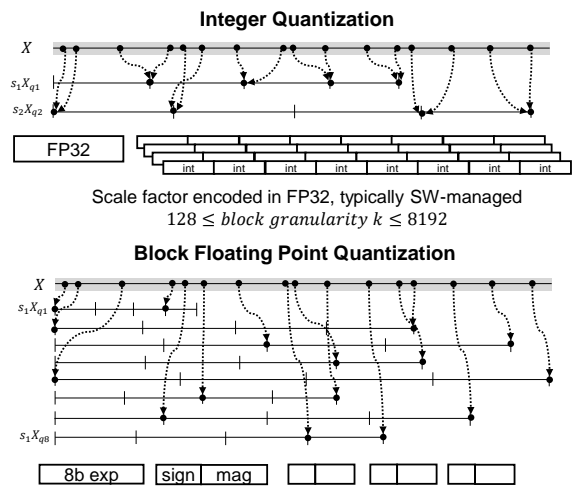


Fig. 3: BFP and INT-based quantization operate on similar principles, but BFP offers superior resolution and numeric fidelity through fine-grained, hardware-managed scaling factors.

increasing the precision of scale factors adds to the cost of implementation and encoding.

As illustrated by the example in Figure 2, a two-level scaling approach enables an approximation of more accurate full-precision scaling. A set of initial values are globally scaled using an “expensive” (amortized over k) FP32 rescaling step based on the data distribution. Pre-scaled partitions X_1 and X_2 are then formed and can be further scaled “cheaply” using scaling factors ss_1 and ss_2 that are constrained to low-cost, power-of-two representation. Comparisons of forms that leverage a two-level scaling approach, as shown in Figure 4, expose a larger design space than previously seen with INT- and BFP-based approaches. Table I summarizes all major techniques and how they differ in choices of encoding scaling (s) and sub-scaling (ss) factors, and block granularity (k_1, k_2).

Narrow-precision Floating-Point (FP8). The FP8 quantization approach, recently popularized by Nvidia [37], [40], relies on a hybrid of hardware-software hierarchical scaling. The FP8-based approach can be interpreted as a two-level scaling approach, where the high-level scale factor s , is maintained

TABLE I: Unification and classification of multiple quantization approaches under the two-level scaling framework. In our notation, $z \in \mathcal{Z}$ and 2^z indicates powers of two.

	Scale	Sub-scale	s type	ssi type	k_1	k_2
INT	SW	-	FP32	-	$\sim 1K$	-
MSFP/BFP	HW	-	2^z	-	~ 10	-
FP8	SW	HW	FP32	2^z	$\sim 10K$	1
VSQ	SW	HW	FP32	INT	$\sim 1K$	~ 10
MX	HW	HW	2^z	2^z	~ 10	~ 1

by the Transformer Engine (a statistical-based heuristic for estimating scale factors) over a coarse granularity such as a tensor (up to $\sim 10K$), while compact sub-scale factors per element (effectively at $k_2 = 1$) are constrained efficiently to powers of two that are privately stored for each element.

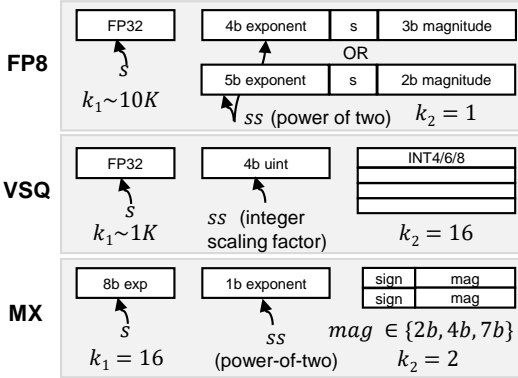


Fig. 4: Three examples of two-level scaling with wide differences. The MX format (this work) uses extremely fine-grain sub-scale factors in the form of hardware-managed shared microexponents to reduce numeric noise at low silicon cost.

Per-Vector Scaled Quantization (VSQ). Another variant of two-level scaling is VSQ [23], which leverages per-vector integer scale factors within accelerator hardware. VSQ uses a coarse-grained software-driven scaling factor with $k_1 \sim 1K$, while also applying a second-level INT-encoded scaling factor ssi over 16 elements of INT4, INT6, or INT8. This approach requires additional logic to handle integer rescaling at a fine granularity within an AI accelerator’s dot product unit.

Shared Microexponents. An extreme variant based on the concept of shared microexponents (MX), which Section IV proposes and evaluates in detail, occupies a new point in the two-level design space with extremely granular parameters $k_1 = 16$ and $k_2 = 2$ with very narrow mantissa as low as two bits. As explained in Section IV, variants of MX offer superior numerical fidelity normalized to silicon cost over previously proposed two-level schemes.

Block Data Representations. As illustrated in Figure 5, the BDR framework generalizes the two-level scaling examples by dividing a global partition of size k_1 into multiple sub-partitions of equal-sized k_2 values. A global scaling factor s is applied to all partitions for rescaling, while the sub-scale factors ssi_i are quantized for efficient storage and computation and applied only to each respective local i^{th} partition.

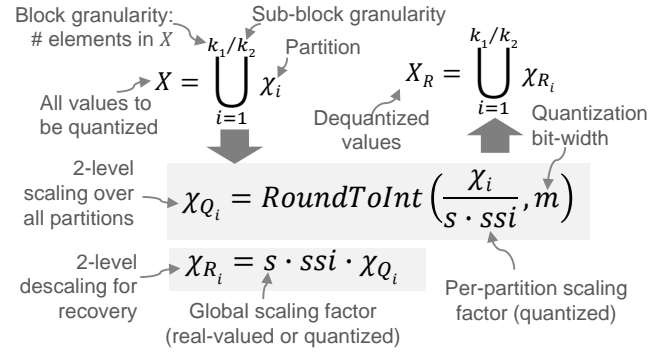


Fig. 5: Two-level scaling and descaling with BDR.

The total number of bits per element in BDR is $(m + 1) + d_1/k_1 + d_2/k_2$, where m represents the explicit mantissa bit-width¹ and d_1 and d_2 represent the number of bits per individual scaling factor s and sub-scaling factor ssi , respectively. Increasing k_1 and k_2 while decreasing m , d_1 , and d_2 is desirable to reduce encoding and compute overheads. However, the quantization noise is minimized by increasing m , d_1 , and d_2 , while decreasing k_1 and k_2 . The dueling tensions across these sets of parameters are explored in Section IV.

While outside the scope of this initial exploration, BDR can naturally extend beyond two levels, with the MX variants as prime candidates. Currently, MX selects compact powers-of-two representations for both the global (s) and local (ssi) scaling factors that trades off scaling precision and flexibility for lowered implementation costs. This scheme could be improved further by introducing an even higher-level parent global scaling factor in software using high-precision FP32 scaling factors over an even coarser granularity at up to $\sim 1K$. MX also currently does not incorporate non-uniform approaches such as log-based representations or lookup tables, or the use of other quantization formats for scaling factors. These explorations are left for future work.

IV. DESIGN SPACE EXPLORATION

In this section, we first formalize the design space as a function of numerical fidelity and hardware cost. We then conduct an exhaustive sweep of BDR design variables consisting of more than 800 configurations to identify the Pareto-optimal design points.

A. Numerical Fidelity

To evaluate the numerical fidelity of BDR configurations, we adopt two approaches. The first is a statistical analysis to investigate the sensitivity of BDR to each design variable and how they contribute to the overall numerical robustness under different data distributions. This allows us to conduct an extensive search over the design space without running costly experiments for every configuration.

In addition to the statistical analysis, we conduct end-to-end training of various scale language models using different

¹Scalar floating-point formats have an implicit leading 1 by design. The variable m in this formula does not account for this implicit bit.

BDR configurations. We find a strong Pearson correlation [50, Ch. 5.1] between the results of our statistical analysis and the language model loss achieved in our end-to-end training runs in the narrow bit-width regime. This suggests that our statistical results are a reliable predictor of the relative numerical fidelity performance of different configurations in practice at single-digit bit-widths.

In our statistical analysis, we use Quantization Signal to Noise Ratio (QSNR) as a measure of numerical fidelity under different quantization schemes. QSNR is defined as the ratio of the power of the non-quantized signal (i.e., the original vector $\mathbf{X} = [x_1, x_2, \dots, x_k] \in \mathbb{R}^k$) to the power of the quantization noise expressed in decibels. It is calculated as:

$$\text{QSNR} := -10 \log\left(\frac{\mathbb{E}[\|Q(\mathbf{X}) - \mathbf{X}\|^2]}{\mathbb{E}[\|\mathbf{X}\|^2]}\right), \quad (3)$$

where $\|\mathbf{X}\| := (\sum_{i=1}^k x_i^2)^{1/2}$, and $Q(\cdot)$ is the quantization function which maps k -dimensional arrays with FP32 precision to the target quantization format. A higher QSNR value indicates that the quantized vector better preserves the direction and magnitude of the original non-quantized vector in the space \mathbb{R}^k . The required QSNR level for a successful training run varies depending on the task complexity, dataset, and model topology. In Section IV-C, we explore the trade-off between hardware efficiency and QSNR for different quantization schemes.

B. Hardware Cost

In this section, we outline a hardware architecture that supports operations on BDR formats and describes our methodology for estimating the costs of these operations in circuit area, power consumption, and memory.

Dot Product Architecture. Figure 6 shows the hardware architecture of a floating-point dot product unit, which can be configured to support various scalar floating-point and MX formats. In addition to the parameters that define the BDR variants of interest (referred to as MX in Table II), the dot product unit in Figure 6 is also parameterized by the dot product length r and the fixed-point reduction accumulation precision f . When the block granularity is greater than 1 (i.e., $k_1 > 1$), the first part of the pipeline reduces the Hadamard product of k_1 elements to a single element. There are r/k_1 such reductions. The results of these r/k_1 reductions are then normalized to the largest element and reduced in fixed-point in the second half of the pipeline. When the block is further broken down to a second-level of granularity (i.e., $k_2 > 1$), the pipeline performs a conditional right-shift, up to $2^{d_2} - 1$ bits, at the depth of $\log_2(k_2)$ while summing the k_1 elements.

In Figure 6, when the pipeline is configured with $k_1 = k_2 = 1$, it implements a standard scalar floating-point dot product. In this setting, the internal accumulation across the native reduction dimension is performed by normalizing the elements of a Hadamard product to the largest element and reducing in fixed-point. This is an optimistic approximation for scalar floating-point area overhead given that the data is

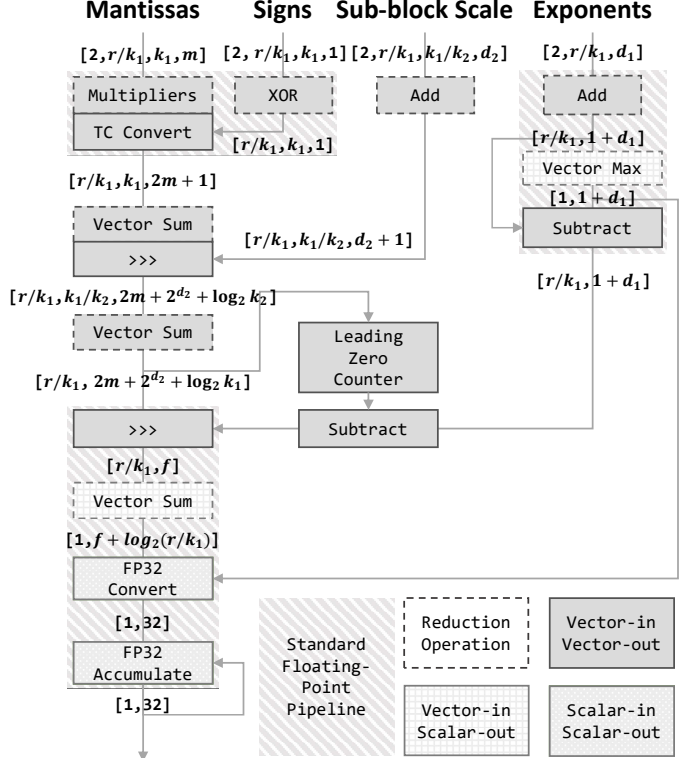


Fig. 6: Typical hardware dot product pipeline used to model variants under the BDR model such as FP, BFP, and MX. We use a separate pipeline (not shown here due to space limitations) for settings that require a second-level INT-based scaling (e.g., VSQ). r represents the reduction dimension of the dot product. Changing the parameters of this pipeline also implements conventional scalar floating-point ($k_1 = k_2 = 1$) and block floating-point ($d_2 = 0$) dot product. The annotations in brackets represent the shape of each input or output to each hardware block. The right-most dimension is the number of bits. In our evaluations, we select f to be the smaller of 25 or the maximum possible dynamic range for each format.

serially accumulating in a floating-point type $f - 2$ mantissa bits instead of building a full floating-point adder tree.

Synthesis and Area Estimation Methodology. In the process of ASIC synthesis and physical design, various parameters can affect the circuit area and power consumption. For instance, synthesis tools can map adders and other blocks into circuits that reduce critical path delay at a cost of increased area [54]. In addition, multi-format dot product units in commercial implementations may share some sub-circuits across different data formats to save on circuit area.

The BDR format is designed to be compatible with existing standard floating-point dot product pipelines in order to enable sub-circuit sharing and lower marginal costs. However, the cost of integrating BDR into a given design will depend on various factors, such as the underlying architecture, the set of data formats, and the relative throughputs of the existing design. To make the results of our synthesis and area estimation methodology more comparable, we normalize the standard-cell area of each BDR configuration to a baseline configurable FP8 dot product unit supporting both E4M3 and E5M2. This allows us to directly compare the relative costs of different

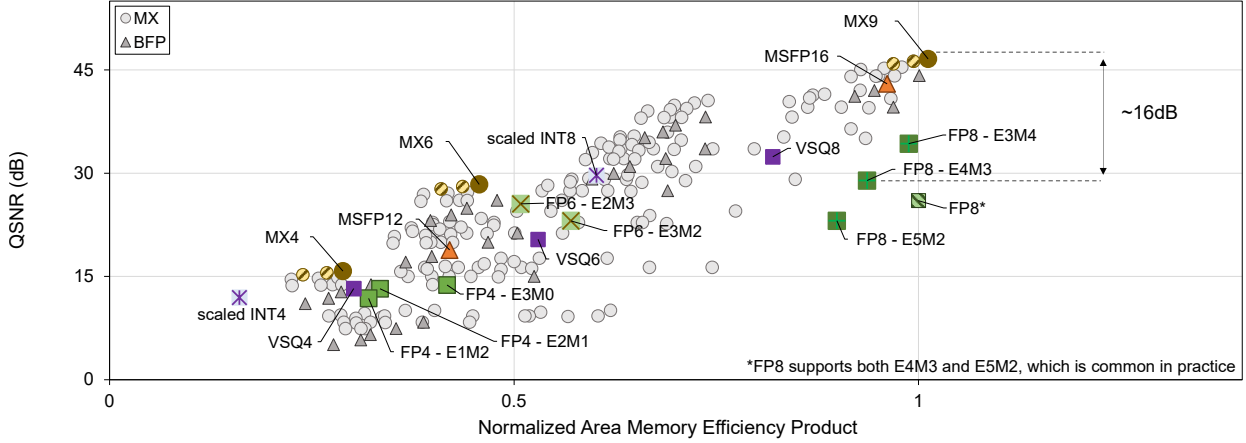


Fig. 7: QSNR vs. the area-memory efficiency product for different BDR configurations. We focus our search space on symmetric dot product units. The area is normalized to a 64-element FP8 dot product and the memory efficiency is the inverse of the packing efficiency of a 256-element tile into a 64B memory interface. We chose a data distribution ($\mathbf{X} \sim \mathcal{N}(0, |\mathcal{N}(0, 1)|)$) that is commonly found in DNN workloads. The conventional block floating-point data format is a subset of BDR with $d_2 = 0$ and is therefore a part of our BDR parameter search. MSFP12 and MSFP16 are instances of the conventional block floating-point proposed in [24]. For integer (INT), VSQ [23], and scalar Floating-Point (FP) formats, we used FP32 first-level scaling factor based on the absolute maximum value over a window of past observed vectors similar to the “delayed scaling” approach proposed [40] for scaling dynamic tensors with varied distribution. VSQ [23] variants shown in this figure are the best of $d_2 = \{4, 6, 8, 10\}$.

BDR configurations and understand the trade-offs between numerical fidelity and hardware cost.

Due to software license usage restrictions, building hundreds of configurations and finding the optimal pipelining for each of them was not feasible. Our research on optimal register placements in smaller sweeps, however, shows that registers typically only accounted for about 10% of the total area. Therefore, a design requiring half as many pipeline stages would only save around 5% of the core area. To isolate the core area for a given configuration from differences in optimal pipeline stage placement or sub-circuit synthesis mapping, we synthesize each configuration with an easily achievable timing constraint of 10ns and with only inputs and outputs being registered. This ensures that synthesis implementation selection targets the minimum area in all designs. We use Synopsys Design Compiler and a leading-edge process node.

Memory Footprint. While it is important to consider the area cost of the dot product unit, we should also consider the memory efficiency — both from a capacity and bandwidth perspective. In particular, the DRAM or High Bandwidth Memory (HBM) interfaces are of a fixed width, therefore while accessing the tensors if the data cannot be packed into the memory interface width, the effective memory capacity and/or bandwidth will be reduced which may result in lower performance (especially for inference use cases). Typical hardware architectures utilize tiling of the input tensors to achieve high performance on AI workloads. Therefore, for the memory footprint analysis, we consider the packing efficiency of a typical tile size of 256 elements (although this is a hardware architecture design variable) into a 64B memory interface.

C. Pareto-frontier formats

Figure 7 illustrates the trade-off between numerical fidelity and the hardware cost for different data format configurations.

The x-axis indicates the implementation cost of each configuration as a function of the dot product area and memory efficiency. The reported QSNR (in decibels) on the y-axis is the averaged measured QSNR from over 10K independent vectors drawn from a normal Gaussian distribution with a variable variance (higher QSNR is better). We chose this distribution to cover a range of variances observed in gradient, error, weight, and activation tensors in a typical training cycle.

In our efficiency analysis, we normalize the dot product area to that of a baseline FP8 (supporting both E4M3 and E5M2) implementation and calculate the memory efficiency as the inverse of the ratio of the number of elements that can be packed into a 64B memory interface. Since the goal is to select a congruent data format for both training and inference, we give equal weight to the dot product area and memory efficiency as they are both important from a performance and power perspective for the two scenarios.

BDR QSNR Lower-Bound. In Figure 7, we analyzed the QSNR of various BDR configurations for a Gaussian distribution with varying variance. Theorem 1 asserts a lower-bound on the QSNR of BDR formats as a function of the number of mantissa bits m , the block granularity k_1 and k_2 , and scale bit-width d_1 and d_2 .

Theorem 1: Given an N -dimensional vector \mathbf{X} drawn from an arbitrary distribution ρ in FP32 precision, the QSNR of the BDR-quantized version of \mathbf{X} is lower-bounded by the following. Variable d_1 is set to 8 for BDR data format and β is an intermediate variable equal to $2^{d_2} - 1$:²

$$\text{QSNR} \geq 6.02 m + 10 \log \left(\frac{2^{2\beta}}{\min(N, k_1) + (2^{2\beta} - 1)k_2} \right). \quad (4)$$

²In general terms, d_2 denotes the minimum number of required bits to represent the difference between the global scaling factor s and the smallest sub-scale factor among ssi 's.

A detailed proof of Theorem 1 can be found in Section IX. As also observed empirically in Figure 7, the QSNR has a linear relation with the number of mantissa bits m and a logarithmic relation with the block granularity k_1 and k_2 . Note that Eq. (4) provides a parameterized lower-bound for the BDR family of data formats. This in turn provides a guarantee of the worst-case numerical fidelity of BDR formats in the face of skewed distributions with correlated noise.

Basic Data Formats. To evaluate the efficacy of BDR data formats on AI workloads in the rest of this paper, we select three representative points from the Pareto frontier in Figure 7. The selected configurations are defined in Table II and are referred to as MX9, MX6, and MX4. We select a format (MX6) whose QSNR is comparable to that of FP8 but with approximately $2\times$ lower area-memory cost. We also select two formats whose QSNR are roughly 50% higher (MX9) and 50% lower (MX4) compared to that of FP8, with comparable and $4\times$ lower area-memory cost, respectively.

The specific parameters of these formats (see Table II) are chosen at the “knee” (shown as hashed points on the Pareto frontier in Figure 7) of a particular parameter’s sweep by trading off the increase in QSNR with the increase in the normalized area-memory efficiency product. For instance, across all the selected formats, increasing the value of d_2 from 1-bit to 2-bit increases the QSNR by only $0.5dB$, but with a $30 - 50\%$ increase in the normalized cost. Similarly, with a d_2 value of 1, reducing k_2 from 8 to 2 increases the QSNR by approximately $2dB$, with only a marginal 3% increase in the normalized cost. Whereas, further reducing the value of k_2 from 2 to 1 increases the QSNR only by $0.7dB$, but with a significant $30 - 40\%$ increase in the normalized cost. We pragmatically select a first-level block granularity of 16 to avoid forcing a large reduction dimension on hardware architectures. In general, we also observe that the trade-off between the increase in the QSNR versus the increase in the normalized area-memory efficiency product reduces as we increase the number of bits per element.

TABLE II: Definition of three basic MX data formats. Both scaling factors d_1 and d_2 are encoded as power-of-two exponents.

		MX9	MX6	MX4
Block granularity	1st level	k_1	16	16
	2nd level	k_2	2	2
Scale bit-width	1st level	d_1	8	8
	2nd level	d_2	1	1
Mantissa bit-width	m	7	4	2
Average bits per element		9	6	4

Even though MX9 is not necessarily on the Pareto frontier in Figure 7, it is still a good choice for the basic data format for further evaluation as it allows all the selected formats to have the same settings (see Table II) except for their mantissa bit-widths, which allows for maximum hardware reuse. Moreover, the difference in QSNR ($\approx 0.8dB$) between the selected MX9 format and the configuration on the Pareto frontier is insignificant for the efficacy of the end-to-end training and inference workloads due to its already high QSNR value. Note that MX9 has approximately $3.6dB$ higher QSNR

compared to that of MSFP16 [24]. Empirical measurements of proprietary generative inference models (results not reported) show a significant accuracy degradation in MSFP16 as a drop-in replacement option that is not occurring in MX9.

MX9 has a hardware efficiency close to that of FP8 with significantly higher numerical fidelity. For instance, in the case of a Gaussian distribution with variable variance, the QSNR of MX9 is about $16dB$ higher than FP8 (E4M3). A $16dB$ higher fidelity is roughly equivalent to having 2 more mantissa bits in the scalar floating-point format. For the same distribution, MX6’s QSNR lies between the two FP8 variants E4M3 and E5M2 while providing an approximately $2\times$ advantage on the hardware cost as measured by the normalized area memory efficiency product. We qualitatively observed a similar trend under different data distributions as well.

V. COMPUTE FLOW

In this section, we describe the computation process for training and inferencing with the MX data format.

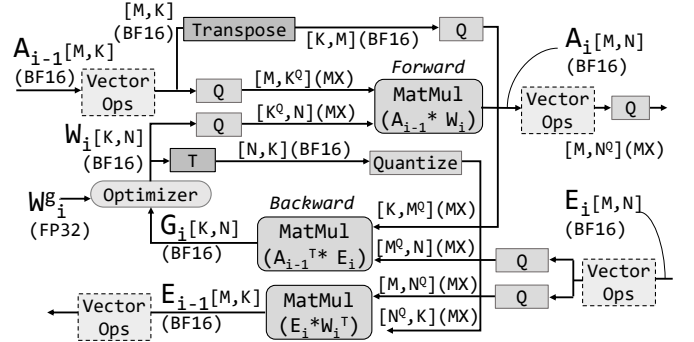


Fig. 8: Compute flow graph of a training iteration including the forward and backward passes with MX quantization. The superscript “Q” in the dimensions (e.g., “MX[K, M^Q]”) indicates the axis along which the tensor is quantized.

Training. Figure 8 illustrates the computation flow of a training iteration using MX format. Tensor reduction operations, such as matrix multiplications and convolutions, are performed in MX during both the forward and backward passes. Both inputs of a tensor operation are MX-quantized. Element-wise operations, such as Layernorm, Softmax, GELU, and residual addition are performed in a scalar floating-point format like BF16 [33] or FP32. In our experiments, we use BF16 as the default data format for element-wise operations with the exception of the vector operations in the diffusion loop and the Softmax in the mixture-of-experts gating function [30].

MX is a directional data format that requires tensors to be quantized along the reduction dimension to attain hardware benefits. This association with a particular dimension means that MX quantization and the transpose operation are not commutative. In the weight update stage, as shown in Figure 8, two quantized versions of the weights are generated: one for the forward pass and one for the backward pass. The transpose operation must be performed before quantizing the weights for the backward pass. Note that both copies do not need to be

TABLE III: Training and inferencing with MX data formats. MX9 can be used as a drop-in replacement for high-precision data formats like FP32 or BF16 in the training and inferencing pipeline without the dependency on complex online statistical heuristics or any change in the hyper-parameter settings. The results of direct casting to MX6 format are also included in this table for completeness. The delta in MX training accuracies (both higher and lower) are typically within the run-to-run variation of FP32-based training when initialized with different random seeds or trained in different containers. The baseline accuracy numbers reported in this table are the FP32 accuracy obtained under the same setting in which MX training is run (exact same seed, container, and node) and not the averaged accuracy under multiple runs. MX6 provides roughly $2\times$ improvement over FP8 in terms of area-memory efficiency and achieves inferences results close to FP32 accuracy with a modest level of quantization-aware fine-tuning.

Task	Family	Model	Dataset	Metric	Training		Inferencing		
					Baseline FP32	MX9	Direct Cast (MX9)	Direct Cast (MX6)	QA Fine-tuning (MX6)
Language Translation	Transformer (Enc-Dec)	Transformer-Base [14]	WMT-17 [7]	BLEU Score \uparrow	26.85	26.51	26.55	26.32	26.81
		Transformer-Large [14]			27.63	27.77	27.60	27.48	27.62
	LSTM	GNMT [8]			24.44	24.47	24.45	24.45	-
Language Encoding	Transformer (Enc-Only)	BERT-Base [12]	Wikipedia [16]	Perplexity \downarrow	4.58	4.62	See Table V for detail.		
		BERT-Large [12]			3.58	3.58			
Language Modeling	GPT (Dec-Only)				See tables VII and IV for detail.				
Image Classification	Vision Transformer	DeiT-Tiny [2]	ImageNet ILSVRC12 [9]	Top-1 Acc. \uparrow	72.16%	72.84%	72.2%	71.23%	71.96%
		DeiT-Small [2]			80.53%	80.31%	80.52%	80.07%	80.34%
	CNN	ResNet-18 [1]			70.79%	70.44%	70.80%	69.35%	70.74%
		ResNet-50 v1.5 [1]			77.41%	77.09%	77.16%	75.63%	77.00%
		MobileNet v2 [13]			72.14%	71.56%	71.48%	67.64%	71.25%
Denoising Diffusion	UNET	Conditioned DDPMP [10]	ImageNet-64 [5]	FID. \downarrow Inception Score \uparrow	7.60 34.76	5.37 34.14	7.81 37.40	26.62 27.88	15.72 31.77 ^a
		Unconditioned DDPMP [10]			21.99 15.34	21.46 15.72	17.79 15.83	44.74 13.10	29.55 15.47
Speech Rec.	Transformer	Wav2Vec 2.0 [15]	LibriSpeech [11]	WER \downarrow	18.9	17.27	18.94	20.98	20.13
Recommendation	MLPs	DLRM [3]	Criteo Terabyte [4]	AUC \uparrow	0.8028	0.8026	0.8027	0.8013	-

^aFID score is a statistical metric used to compare the distribution of generated images compared to a reference set. FID is known to have a high variance sensitive to data, image size, etc. Inception score, on the other hand, evaluates the distribution of the generated images and has less variance.

stored in working memory at the same time unless a very fine-grained interleaving of the forward and backward passes (or recompute strategy) is deployed.

Inferencing. Narrow bit-width deployment is made easier with MX data format as training and inferencing use the same congruent data format. In Section VI, we also evaluate the use of MX for inferencing models trained in other formats. For post-training quantization, we consider two scenarios:

Direct cast (drop-in replacement). In this setting, we take a pre-trained model in higher precision (e.g., FP32, BF16, and FP16), perform a straight cast into MX data format, and evaluate the model quality.

Quantization-aware fine-tuning. In this setting, we take a pre-trained model in higher precision (e.g., FP32, BF16, and FP16), cast it into MX format, and perform a few iterations of quantization-aware fine-tuning to recover any potential accuracy drop. This approach is mostly used for inferencing with narrower data formats like MX6 and MX4. The compute flow for the fine-tuning step is similar to that shown in Figure 8, except that the forward and backward passes may use different bit-widths. For example, the forward pass might use MX6 or MX4 and the backward pass might use a higher bit-width format (e.g., MX9, BF16, or FP32).

In memory-intensive scenarios such as recommendation models, we can further improve inferencing performance by quantizing both storage and compute to MX format. In our evaluation of the DLRM model in Section VI, we leverage this optimization by quantizing both the embedding tables and tensor computations to MX format.

VI. EMPIRICAL RESULTS

Experimental Setup. In our evaluations, we use a custom CUDA library to emulate MX data formats on current GPU

architectures. Our custom CUDA library reproduces numerical results identical to what a native-MX silicon would produce. All tensor operations in forward and backward passes are performed with the MX data format (including the first and last layers) unless explicitly called out otherwise.

A. Benchmarks

To evaluate the quality of MX data formats, we created a comprehensive benchmark suite featuring over 20 representative open-source and proprietary AI models. Our benchmark suite includes a diverse range of model architectures and covers a wide range of modalities. In the following, we provide an overview of the models in our benchmark suite.

Text and Natural Language. Natural Language Processing (NLP) is a key area of research in deep learning. NLP applications can be roughly broken down into three subsets:

- *Neural Machine Translation.* This application is focused on translating text from one language to another. We evaluate two model topologies in this category: LSTM-based and transformer-based. For the LSTM-based model, we use the MLPperf GNMT-V2 model [55]. The transformer-based benchmark is based on the work of [52] and includes two variants: Transformer-base and Transformer-big. These models are trained using the WMT17-EN-DE data [19] and evaluated on the WMT14-EN-DE [20].
- *Text Encoding and Language Understanding.* For this application, we evaluate the popular BERT [28] models: BERT-base and BERT-large. The models are trained on the Wikipedia data and evaluated on SQuAD-v1.1 [45].
- *Generative Language Modeling.* The goal of generative language modeling is to produce the next word given the prior sequence. Auto-regressive generative learning is probably

TABLE IV: Zero-shot and few-shot inferencing with MX data format on the OpenAI GPT3-175B model [21]. All the reported accuracies are the results of a “**direct cast**” into MX format with no quantization-aware fine-tuning. The tuple (w, a) indicates the format used for weights and activation. Note that few-shot accuracy in ANLI-r2 is lower than zero-shot accuracy due to the nature of this task.

Task	N-shot	Baseline FP32	(MX9, MX9)	(MX6, MX9)	(MX6, MX6)	(MX4, MX9)	(MX4, MX6)	(MX4, MX4)
Hellaswag	0	76.2 \pm 0.4	76.2 \pm 0.4	76.0 \pm 0.4	75.8 \pm 0.4	74.5 \pm 0.4	74.0 \pm 0.4	61.3 \pm 0.5
	1	76.5 \pm 0.4	76.6 \pm 0.4	76.3 \pm 0.4	76.0 \pm 0.4	74.0 \pm 0.4	73.6 \pm 0.4	59.1 \pm 0.5
	2	77.4 \pm 0.4	77.3 \pm 0.4	77.3 \pm 0.4	76.8 \pm 0.4	74.8 \pm 0.4	74.3 \pm 0.4	59.4 \pm 0.4
WIC	0	48.3 \pm 2.0	47.8 \pm 2.0	48.0 \pm 2.0	48.1 \pm 2.0	48.9 \pm 2.0	48.0 \pm 2.0	50.3 \pm 2.0
	1	50.9 \pm 2.0	50.8 \pm 2.0	51.4 \pm 2.0	50.3 \pm 2.0	49.1 \pm 2.0	47.5 \pm 2.0	46.9 \pm 2.0
	2	50.5 \pm 2.0	50.5 \pm 2.0	50.5 \pm 2.0	50.6 \pm 2.0	48.9 \pm 2.0	49.7 \pm 2.0	52.2 \pm 2.0
Anli-r2	0	35.6 \pm 1.6	35.2 \pm 1.5	36.6 \pm 1.5	36.2 \pm 1.5	34.0 \pm 1.5	34.3 \pm 1.5	35.8 \pm 1.5
	1	33.8 \pm 1.5	33.7 \pm 1.5	33.4 \pm 1.5	32.8 \pm 1.5	33.0 \pm 1.5	33.3 \pm 1.5	31.7 \pm 1.5
	2	34.5 \pm 1.5	33.9 \pm 1.5	34.0 \pm 1.5	35.5 \pm 1.5	34.1 \pm 1.5	34.2 \pm 1.5	33.0 \pm 1.5
Winogrande	0	70.8 \pm 1.3	71.0 \pm 1.3	71.1 \pm 1.3	70.7 \pm 1.3	71.5 \pm 1.3	70.2 \pm 1.3	66.1 \pm 1.3
	1	73.0 \pm 1.3	72.2 \pm 1.2	71.6 \pm 1.2	71.5 \pm 1.2	71.4 \pm 1.2	71.4 \pm 1.2	64.1 \pm 1.2
	2	74.0 \pm 1.2	74.3 \pm 1.2	73.8 \pm 1.2	74.9 \pm 1.2	72.9 \pm 1.2	72.5 \pm 1.2	61.7 \pm 1.2

the most significant and fastest-growing application in the NLP domain. In our benchmark suite, we evaluate MX performance on a variety of dense Generative Pre-Trained Transformers (GPT) models of size $6M$ up to $175B$. All models are trained with a sequence length of 1024 to efficiency with the number of tokens processed estimated by GPT scaling power laws [35]. In addition to dense GPT models, we also evaluate an example Mixture-of-Experts (MoE) generative model from [44]. The MoE model in our study has $1.9B$ parameters with 12 layers, a hidden dimension of 768, 12 attention heads, and 64 experts. The model is trained with 2048 sequence length for $40B$ tokens.

Computer Vision. Image classification and image generation are two important applications in computer vision:

- *Image Classification.* We evaluate three main families of models for image classification: ResNet [32], MobileNet-v2 [46], and DeiT [51]. From the ResNet family, we use two popular variants, ResNet-18 and ResNet-50. We also evaluate two variants of vision transformers (a.k.a., DeiT) in our assessment. All image recognition benchmarks are trained and validated with ImageNet ILSVRC12 data [25].
- *Image Generation.* Image generation involves creating new, previously unseen images using deep learning techniques. We use the DDPM model [39] as a representative model in this category. We evaluate two variations of the DDPM model. The first is an unconditional model with 128 channels and a hybrid loss function, and the second is a class-conditional model with 192 channels. Both models are trained with 4000 diffusion steps using ImageNet-64.

Audio and Speech. Speech recognition involves transcribing spoken language into text. In our benchmark suite, we evaluate the Wave2Vec 2.0 model [18], which is one of the current leading models using self-supervised training. We use the base configuration of Wave2Vec 2.0 in our evaluations. Librispeech data [41] is used to train and evaluate this model.

Categorical Data. One of the industrial applications of deep learning is processing categorical data in recommendation systems. In our benchmark suite, we include the MLperf Deep Learning Recommendation Model (DLRM) [38] in addition

TABLE V: Question-Answering using BERT. Each entry reports **Exact Match / F1 score**. In both benchmarks, no quantization-aware fine-tuning is needed even with the MX6 data format.

Model	Baseline FP32	Direct Cast (MX9)	Direct Cast (MX6)
Bert-Base	80.80 / 88.46	80.71 / 88.45	80.62 / 88.36
Bert-Large	87.65 / 93.48	87.63 / 93.45	87.49 / 93.37

to three internal production models. We refer to these internal models as PR-rec1, PR-rec2, and PR-rec3. The models are trained on large-scale internal data with tens or hundreds of billion samples collected from online recommendation services. PR-rec1 utilizes the canonical DLRM architecture at a much larger scale than open-source models, with nearly 1000 embedding tables and over 100 fully-connected layers. This model, with 32-bit parameters, amounts to several terabytes in size. PR-rec2 and PR-rec3 use different interaction architectures compared to the DLRM, with PR-rec2 using transformer-based encoders and PR-rec3 using DHEN [57].³

B. Inferencing with the MX data format

Tables III to V summarize the MX inferencing results in both direct casting and quantization-aware fine-tuning settings across a variety of model topologies, scales, and modalities. As shown, a direct cast to MX9 might be used as a drop-in replacement alternative to high-precision FP32/BF16/FP16 in a wide range of applications.

Direct casting to the more efficient MX6 format sometimes causes model accuracy to degrade. In these cases, the loss in accuracy can be recovered through a modest amount of quantization-aware fine-tuning. We report both the direct cast and fine-tuning results for MX6 in Tables III and V. We generally saw the best quantization-aware fine-tuning results when we reset the optimizer, adjusted the initial learning rate, and eliminated rate decay, dropout, and momentum. In all our fine-tuning experiments, we use FP32 for the backward pass. The amount of fine-tuning necessary varied across benchmarks but was always much shorter than the original training duration.

³The evaluation on the production recommendation models is done as part of a collaboration between Meta and Microsoft. All the evaluations on the rest of benchmarks are performed by Microsoft.

The MX data format also presents opportunities for optimizing zero-shot and few-shot generative inferencing with no task-specific fine-tuning. See Table IV for quantization results of OpenAI GPT3-175B model with MX formats. Consistent with the results for discriminative inferencing reported in Table III, MX9 provides a drop-in replacement alternative for efficient generative inferencing. Generative inferencing at large-scale allows the use of even narrower data formats such as MX4 and MX6 without the need for much quantization-aware fine-tuning. To the best of our knowledge, this is the first work reporting high-quality generative inferencing with both weights and activations quantized to ultra-narrow bit-width through a direct cast. In prior quantized generative inferencing work, the activation is typically kept at high precision BF16/FP16 and only weights are being quantized [27], [42]. This is because INT8/INT4 quantization of activations usually requires careful offline outlier suppression [56] to achieve reasonable results.

C. Training with MX data format

MX9 provides a robust drop-in replacement for high bit-width AI training (i.e., FP32/BF16/FP16) without requiring an outlier detection heuristic or any change in the training recipe, hyper-parameters, or model topology. Table III provides an overview of MX9 training results for a variety of discriminative benchmarks across different model topologies and data modalities. The results show that the models trained with MX9 match FP32 baseline accuracy within the error margin of run-to-run FP32-based training when initialized with different random seeds. The work in [37] reports FP8 results on a subset of these benchmarks.

In addition to benchmarks listed in Table III, we further evaluated the robustness of MX9 training on three proprietary recommendation models. Table VI summarizes the results of this evaluation. Consistent with the results of our open-sourced benchmark suite, MX9 presents a robust training alternative for production-scale recommendation models. In our experience, FP8-based training led to gradient explosion in PR-rec3 models while MX9 had a robust convergence trend.

TABLE VI: Normalized [cross] Entropy (NE) difference of MX9 training and baseline FP32 for different recommendation models. In the mixed-precision training of PR-rec3, > 99% of the compute in forward/backward passes is still in MX9. In PR-rec2 mixed-precision training, > 94% of compute is kept in MX9 format. Note that although uniform MX9 training showed a robust training trend across all 3 models (unlike FP8), for some benchmarks we opt to use a mixed-precision setting to meet the service-level agreements.

Model Name	Model Topology	MX9 Training	Mixed-Precision Training
PR-rec1	DLM	0.02%	N/A
PR-rec2	Transformer	0.05%	0.01%
PR-rec3	DHEN	0.1%	-0.02%

Internally, we use a tight threshold of 0.02% for production models, which is set based on the training variations from run to run with the FP32 format [26]. Training PR-rec1 with MX9 and MX6 can both meet this requirement but MX4 results in higher normalized entropy variation up to 0.07% with the same number of training iterations and hyper-parameters as the baseline FP32. MX6 and MX4 have roughly 2 \times and 4 \times lower

circuitry compared to FP8. We leave further evaluation of MX4 and MX6 for training recommendation models to future work. PR-rec2 and PR-rec3 are more challenging benchmarks to quantize. As shown in Table VI, certain layers (e.g., first and last layer) should be kept in high bit-width to meet the 0.02% threshold.

Table VII shows the result of training generative transformers of various sizes with MX9 format. MX9 matches the quality of FP32 without the need for any heuristic-based outlier detection (e.g., transformer engine in [37]) or change in the training recipe (number of training iterations, hyper-parameters, or model topology).

TABLE VII: Generative training of dense and MoE language models with MX9 matches the language model loss of the FP32 baseline.

Model	Baseline FP32	MX9
GPT-XS (6M)	4.61	4.61
GPT-S (20M)	4.03	4.03
GPT-M (150M)	3.31	3.31
GPT-L (345M)	3.11	3.11
GPT-XL (1.5B)	2.74	2.74
MoE (1.9B)	2.22	2.21

Our assessment of training generative language models with the more efficient MX6 format shows that the models trained with this data format are also able to converge robustly. Figure 9 shows the Language Model (LM) loss as a function of normalized cost per training iteration for MX9 versus MX6. MX6 requires more training iterations compared to the baseline FP32 (and by extension MX9) to converge to the same LM loss. Given the relative throughput of MX6, however, the model can still converge to the same quality as the baseline with an overall lower training cost. Quantifying the exact impact of the MX6 data format on the underlying generative training power laws is out of the scope of this paper.

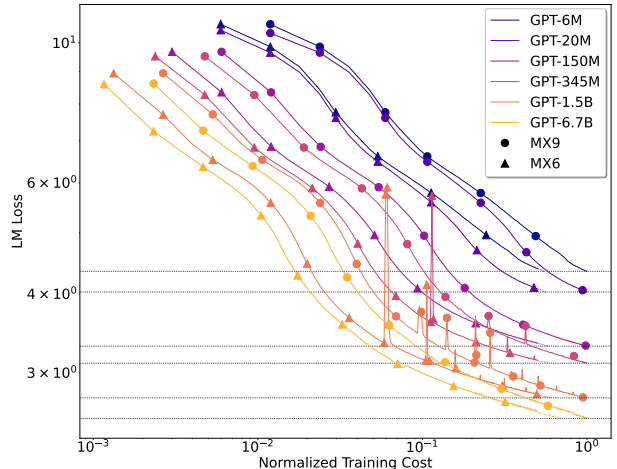


Fig. 9: Training generative language models with MX6 data format. The y-axis shows the LM loss of different-sized GPT models and the x-axis shows the normalized training cost with respect to a MX9 baseline. The cost is approximated based on the expected tensor unit throughput not accounting for the overhead of vector operations. Unlike MX9, training language models with MX6 requires more iterations of training to match baseline accuracy. The additional iterations are shown as dashed lines in MX6 training curves. Dotted horizontal lines show the baseline FP32 LM loss at efficiency.

VII. RELATED WORK

AI training and inferencing using narrow bit-width data formats has become a mainstream industry standard. Prior work in this domain can be grouped into two main categories: classic scalar floating-point and block floating-point.

The most common examples of scalar floating-point formats are BF16 [17], [34], TF32 [48], FP16 [36], and FP8 [37], [49], [53]. While the scaling down of traditional scalar floating-point formats from FP32 to FP8 has been very successful, it is reaching a point of diminishing returns. To continue driving the advancement of AI, there is a need for an alternative approach to further improve the efficiency and robustness of data encoding at narrow bit-widths for AI models.

Several prior works have proposed Conventional Block Floating-Point as a potential alternative to scalar floating-point for AI training and inferencing. The work in [24] provides a detailed analysis of different block floating-point variants and their application for AI inferencing at production-scale. The work in [29] takes a hybrid approach for AI training using BFP. The hybrid BFP recipe is further optimized in [22] by varying the block size and mantissa bit-width across different layers and training epochs. FAST [43] also varies the mantissa bit-width per training iteration and supports this with a bit-serial hardware architecture that multiplies two mantissa bits at a time. In another work [23], authors explored hierarchical BFP with a per-channel floating-point scale and a per-block integer scale to accelerate AI inference. Although promising, to the best of our knowledge, none of the prior work reports a generalizable basic BFP data format that can be used as a drop-in replacement for scalar floating-point, both in terms of model accuracy and usability (i.e., straightforward training recipes and a direct cast option for inferencing).

The unified quantization framework presented in this paper allows reasoning about both scalar and block floating-point under the same design space. Through extensive exploration, we have identified a new family of data formats that provide a better trade-off in terms of fidelity (model accuracy) and hardware cost. The proposed format provides a robust alternative for AI training and inferencing without the need for complex heuristics, or changes in the training or inferencing recipes.

VIII. CONCLUSION

This paper introduces BDR, a general framework for evaluating various quantization schemes. Leveraging BDR, we explore the benefit of shared microexponents in the form of MX formats. We evaluated variants of MX data formats on over 20 benchmarks across different scales, modalities, and model topologies. Our results corroborate the efficacy of BDR data formats as a promising solution for improving the performance of future AI hardware.

IX. PROOF OF THEOREM 1

We first prove Theorem 1 for $N = k_1$ with scale 1 and then extend it to an arbitrary N and scale s . Consider a vector $\mathbf{X} = [x_1, x_2, \dots, x_{k_1}] \in \mathbb{R}^{k_1}$ with maximum exponent E before

being converted to BDR data format. Since E is the maximum shared exponent, all elements x_i can take the binary form

$$\begin{aligned} x_i &= (-1)^{\psi^{(i)}} \times p_0^{(i)} \cdot p_{-1}^{(i)} p_{-2}^{(i)} p_{-3}^{(i)} p_{-4}^{(i)} \cdots \times 2^E \\ &= (-1)^{\psi^{(i)}} \times \left(\sum_{j=0}^{\infty} p_{-j}^{(i)} 2^{-j} \right) \times 2^E, \end{aligned} \quad (5)$$

where $\psi^{(i)} \in \{0, 1\}$, $p_j^{(i)} \in \{0, 1\}$, and $1 \leq i \leq k_1$. E is the private exponent of an element x_κ in \mathbf{X} with the maximum absolute value among x_i 's.

Recall that BDR supports m mantissa bits and 1 sign bit. Since elements in \mathbf{X} are in FP32 precision, which supports 8 exponent bits, E can be represented in its FP32 form. After rounding the mantissa bits to the nearest floating point number with m mantissa bits, we have:

$$Q(x_i) = (-1)^{\psi^{(i)}} \times \left(\sum_{j=0}^{m-1} Q_{-j}^{(i)} 2^{-j} \right) \times 2^E, \quad (6)$$

where $\psi^{(i)} \in \{0, 1\}$, $Q_{-j}^{(i)} \in \{0, 1\}$, and $1 \leq i \leq k_1$. This results into the quantization error:

$$|Q(x_i) - x_i| \leq 2^{E-m}, \quad (7)$$

for all $1 \leq i \leq k_1$. Similarly, the quantization error for elements with sub-block shift of $\tau \leq \beta$ is upper bounded as follows:

$$|Q(x_i) - x_i| \leq 2^{E-\tau-m}. \quad (8)$$

Without loss of generality, assume that r_τ sub-blocks in \mathbf{X} have a sub-block shift of τ . This assumption implies that there exist $\sum_{\tau=0}^{\beta-1} r_\tau k_2$ elements with sub-block shifts smaller than β , since the sub-block size is k_2 . The remaining $k_1 - \sum_{\tau=0}^{\beta-1} r_\tau k_2$ elements in the block have a sub-block shift of β . Thus, according to (8), we have:

$$\begin{aligned} \|Q(\mathbf{X}) - \mathbf{X}\|^2 &= \sum_{i=1}^{k_1} |q(x_i) - x_i|^2 \\ &\leq \sum_{\tau=0}^{\beta-1} r_\tau k_2 (2^{E-\tau-m})^2 + (k_1 - \sum_{\tau=0}^{\beta-1} r_\tau k_2) (2^{E-\beta-m})^2 \\ &= \left(\frac{k_1 + \sum_{\tau=0}^{\beta-1} r_\tau k_2 (2^{2\beta-2\tau} - 1)}{2^{2\beta}} \right) (2^{2E-2m}). \end{aligned} \quad (9)$$

In BDR, at least one element within each sub-block with the sub-block shift of $\tau < \beta$ (not equal to β) should have a private exponent of $E - \tau$. So, there exist at least r_τ elements with private exponent of $E - \tau$ for $\tau < \beta$. Then, the power of signal is lower-bounded as follows:

$$\begin{aligned} \|\mathbf{x}\|^2 &= \sum_{i=1}^{k_1} x_i^2 \\ &\geq \sum_{\tau=0}^{\beta-1} r_\tau (2^{E-\tau})^2 \end{aligned} \quad (10)$$

By combining the bounds in (9) and (10), we have the following inequality for the quantization noise-to-signal ratio:

$$\begin{aligned}
\frac{\mathbb{E}[\|Q(\mathbf{X}) - \mathbf{X}\|^2]}{\mathbb{E}[\|\mathbf{X}\|^2]} &\leq \max_{\mathbf{X} \sim \rho} \frac{\|q(\mathbf{X}) - \mathbf{X}\|^2}{\|\mathbf{X}\|^2} \\
&\leq \frac{(k_1 + \sum_{\tau=0}^{\beta-1} r_\tau k_2 (2^{2\beta-2\tau} - 1))(2^{2E-2m})}{2^{2\beta} \sum_{\tau=0}^{\beta-1} r_\tau (2^{2E-2\tau})} \\
&= \frac{(k_1 + \sum_{\tau=0}^{\beta-1} r_\tau k_2 (2^{2\beta-2\tau} - 1))(2^{-2m})}{\sum_{\tau=0}^{\beta-1} r_\tau (2^{2\beta-2\tau})} \\
&= \left(\frac{k_1}{\sum_{\tau=0}^{\beta-1} r_\tau (2^{2\beta-2\tau})} + k_2 \right. \\
&\quad \left. - \frac{k_2 \sum_{\tau=0}^{\beta-1} r_\tau}{\sum_{\tau=0}^{\beta-1} r_\tau (2^{2\beta-2\tau})} \right) \cdot 2^{-2m} \\
&\leq \left(\frac{k_1}{2^{2\beta}} + k_2 - \frac{h \sum_{\tau=0}^{\beta-1} r_\tau}{\sum_{\tau=0}^{\beta-1} r_\tau (2^{2\beta-2\tau})} \right) \cdot 2^{-2m}.
\end{aligned} \tag{11}$$

Note that the last inequality in (11) holds since at least one sub-block containing x_κ has the sub-block shift of zero; i.e., $r_0 \geq 1$. We can further use the inequality

$$\frac{\sum_{\tau=0}^{\beta-1} r_\tau}{\sum_{\tau=0}^{\beta-1} r_\tau (2^{2\beta-2\tau})} \geq \frac{1}{2^{2\beta}}$$

to streamline (11) as

$$\begin{aligned}
\frac{\mathbb{E}[\|Q(\mathbf{X}) - \mathbf{X}\|^2]}{\mathbb{E}[\|\mathbf{X}\|^2]} &\leq \left(\frac{k_1}{2^{2\beta}} + k_2 - \frac{k_2}{2^{2\beta}} \right) \cdot 2^{-2m} \\
&= \left(\frac{k_1 + (2^{2\beta} - 1)k_2}{2^{2\beta}} \right) \cdot 2^{-2m}
\end{aligned} \tag{12}$$

Converting (12) into the QSNR in (3) leads to:

$$\begin{aligned}
\text{QSNR} &\geq -10 \log \left(\left(\frac{k_1 + (2^{2\beta} - 1)k_2}{2^{2\beta}} \right) \cdot 2^{-2m} \right) \\
&= 10 m \log(4) + 10 \log \left(\frac{2^{2\beta}}{k_1 + (2^{2\beta} - 1)k_2} \right) \\
&\geq 6.02 m + 10 \log \left(\frac{2^{2\beta}}{k_1 + (2^{2\beta} - 1)k_2} \right).
\end{aligned} \tag{13}$$

The lower-bound (13) holds for an arbitrary scale s , since one can change the variable \mathbf{X} to $\frac{1}{s}\mathbf{X}$ and recast the QSNR as

$$\frac{\mathbb{E}[\|sQ(\frac{1}{s}\mathbf{X}) - \mathbf{X}\|^2]}{\mathbb{E}[\|\mathbf{X}\|^2]} = \frac{\mathbb{E}[\|Q(\frac{1}{s}\mathbf{X}) - \frac{1}{s}\mathbf{X}\|^2]}{\mathbb{E}[\|\frac{1}{s}\mathbf{X}\|^2]}.$$

The lower-bound (13) also holds for $N > k_1$ since the noise-to-signal ratio in (12) is effectively averaging across blocks of size k_1 . For $N < k_1$, we are effectively reducing the BDR block size to N which improves the lower-bound if we replace k_1 with N . In summary, the following lower-bound holds for various values of N and scale s :

$$\text{QSNR} \geq 6.02 m + 10 \log \left(\frac{2^{2\beta}}{(2^{2\beta} - 1)k_2 + \min(N, k_1)} \right). \blacksquare$$

REFERENCES

- [1] “Convolutional Network for Image Classification in PyTorch.” [Online]. Available: <https://github.com/NVIDIA/DeepLearningExamples/tree/master/PyTorch/Classification/ConvNets>
- [2] “Data-Efficient architectures and training for Image classification.” [Online]. Available: <https://github.com/facebookresearch/deit>
- [3] “Deep Learning Recommendation Model for Personalization and Recommendation Systems.” [Online]. Available: <https://github.com/facebookresearch/dlrm>
- [4] “Display Advertising Challenge.” [Online]. Available: <https://ailab.criteo.com/ressources/criteo-1tb-click-logs-dataset-for-mlperf/>
- [5] “Downsampled ImageNet 64x64.” [Online]. Available: <https://www.kaggle.com/datasets/ayaroshevskiy/downsampled-imagenet-64x64>
- [6] “Findings of the 2016 Conference on Machine Translation.” [Online]. Available: <http://www.statmt.org/wmt16>
- [7] “Findings of the 2017 Conference on Machine Translation (WMT17).” [Online]. Available: <http://www.statmt.org/wmt17>
- [8] “GNMT v2 For PyTorch.” [Online]. Available: <https://github.com/NVIDIA/DeepLearningExamples/tree/master/PyTorch/Translation/GNMT>
- [9] “ImageNet: A Large-Scale Hierarchical Image Database.” [Online]. Available: <https://image-net.org/challenges/LSVRC/2012/index.php>
- [10] “Improved-diffusion.” [Online]. Available: <https://github.com/openai/improved-diffusion>
- [11] “Librispeech: An ASR Corpus Based on Public Domain Audio Books.” [Online]. Available: <http://www.openslr.org/12>
- [12] “NVIDIA/Megatron-LM: Ongoing research training transformer.” [Online]. Available: <https://github.com/NVIDIA/Megatron-LM>
- [13] “Torchvision MobileNetV2.” [Online]. Available: <https://github.com/pytorch/vision>
- [14] “Transformer For PyTorch.” [Online]. Available: <https://github.com/NVIDIA/DeepLearningExamples/tree/master/PyTorch/Translation/Transformer>
- [15] “wav2vec 2.0.” [Online]. Available: <https://github.com/facebookresearch/fairseq/tree/main/examples/wav2vec>
- [16] “Wikimedia Downloads.” [Online]. Available: <https://dumps.wikimedia.org/enwiki/latest/enwiki-latest-pages-articles.xml.bz2>
- [17] “BFLOAT16 - Hardware Numerics Definition,” 2018, accessed Dec 2022. [Online]. Available: <https://www.intel.com/content/dam/develop/external/us/en/documents/bf16-hardware-numerics-definition-white-paper.pdf>
- [18] A. Baevski, Y. Zhou, A. Mohamed, and M. Auli, “wav2vec 2.0: A Framework for Self-Supervised Learning of Speech Representations,” *Advances in Neural Information Processing Systems (NeurIPS)*, vol. 33, pp. 12449–12460, 2020.
- [19] O. r. Bojar, R. Chatterjee, C. Federmann, Y. Graham, B. Haddow, S. Huang, M. Huck, P. Koehn, Q. Liu, V. Logacheva, C. Monz, M. Negri, M. Post, R. Rubino, L. Specia, and M. Turchi, “Findings of the 2017 Conference on Machine Translation (WMT17),” *Conference on Machine Translation (WMT)*, pp. 169–214, September 2017. [Online]. Available: <http://www.aclweb.org/anthology/W17-4717>
- [20] O. Bojar, C. Buck, C. Federmann, B. Haddow, P. Koehn, J. Leveling, C. Monz, P. Pecina, M. Post, H. Saint-Amand, R. Soricut, L. Specia, and A. Tamchyna, “Findings of the 2014 Workshop on Statistical Machine Translation,” *Conference on Machine Translation (WMT)*, pp. 12–58, 2014.
- [21] T. Brown, B. Mann, N. Ryder, M. Subbiah, J. D. Kaplan, P. Dhariwal, A. Neelakantan, P. Shyam, G. Sastry, A. Askell, S. Agarwal, A. Herbert-Voss, G. Krueger, T. Henighan, R. Child, A. Ramesh, D. Ziegler, J. Wu, C. Winter, C. Hesse, M. Chen, E. Sigler, M. Litwin, S. Gray, B. Chess, J. Clark, C. Berner, S. McCandlish, A. Radford, I. Sutskever, and D. Amodei, “Language Models are Few-Shot Learners,” *Advances in Neural Information Processing Systems (NeurIPS)*, vol. 33, pp. 1877–1901, 2020.
- [22] S. Burcu Harma, C. Sönmez, B. Falsafi, M. Jaggi, and Y. Oh, “Accuracy Boosters: Epoch-Driven Mixed-Mantissa Block Floating-Point for DNN Training,” *arXiv preprint arXiv:2211.10737*, 2022.
- [23] S. Dai, R. Venkatesan, M. Ren, B. Zimmer, W. Dally, and B. Khailany, “VS-Quant: Per-vector Scaled Quantization for Accurate Low-Precision Neural Network Inference,” *Machine Learning and Systems (MLSys)*, vol. 3, pp. 873–884, 2021.

[24] B. Darvish Rouhani, D. Lo, R. Zhao, M. Liu, J. Fowers, K. Ovtcharov, A. Vinogradsky, S. Massengill, L. Yang, R. Bittner, A. Forin, H. Zhu, T. Na, P. Patel, S. Che, L. Chand Koppaka, X. SONG, S. Som, K. Das, S. T. S. Reinhardt, S. Lanka, E. Chung, and D. Burger, “Pushing the Limits of Narrow Precision Inferencing at Cloud Scale with Microsoft Floating Point,” *Advances in Neural Information Processing Systems (NeurIPS)*, vol. 33, pp. 10 271–10 281, 2020.

[25] J. Deng, W. Dong, R. Socher, L.-J. Li, K. Li, and L. Fei-Fei, “ImageNet: A Large-Scale Hierarchical Image Database,” *Conf. on Computer Vision and Pattern Recognition (CVPR)*, pp. 248–255, 2009.

[26] Z. Deng, J. Park, P. T. P. Tang, H. Liu, J. Yang, H. Yuen, J. Huang, D. Khudia, X. Wei, E. Wen *et al.*, “Low-precision hardware architectures meet recommendation model inference at scale,” *IEEE Micro*, vol. 41, no. 5, pp. 93–100, 2021.

[27] T. Dettmers and L. Zettlemoyer, “The case for 4-bit precision: k-bit inference scaling laws,” *arXiv preprint arXiv:2212.09720*, 2022.

[28] J. Devlin, M.-W. Chang, K. Lee, and K. Toutanova, “BERT: Pre-Training of Deep Bidirectional Transformers for Language Understanding,” *arXiv preprint arXiv:1810.04805*, Oct. 2018.

[29] M. Drumond, T. Lin, M. Jaggi, and B. Falsafi, “Training DNNs with Hybrid Block Floating Point,” *Advances in Neural Information Processing Systems (NeurIPS)*, vol. 31, 2018.

[30] W. Fedus, B. Zoph, and N. Shazeer, “Switch transformers: Scaling to trillion parameter models with simple and efficient sparsity,” 2021.

[31] A. Gholami, S. Kim, Z. Dong, Z. Yao, M. W. Mahoney, and K. Keutzer, “A survey of quantization methods for efficient neural network inference,” *arXiv preprint arXiv:2103.13630*, 2021.

[32] K. He, X. Zhang, S. Ren, and J. Sun, “Deep Residual Learning for Image Recognition,” *arXiv preprint arXiv:1512.0338*, Dec. 2015.

[33] D. Kalamkar, D. Mudigere, N. Mellemundi, D. Das, K. Banerjee, S. Avancha, D. T. Vooturi, N. Jammalamadaka, J. Huang, H. Yuen *et al.*, “A study of bfloat16 for deep learning training,” *arXiv preprint arXiv:1905.12322*, 2019.

[34] D. Kalamkar, D. Mudigere, N. Mellemundi, D. Das, K. Banerjee, S. Avancha, D. T. Vooturi, N. Jammalamadaka, J. Huang, H. Yuen, J. Yang, J. Park, A. Heinecke, E. Georganas, S. Srinivasan, A. Kundu, M. Smelyanskiy, B. Kaul, and P. Dubey, “A Study of BFLOAT16 for Deep Learning Training,” *arXiv preprint arXiv:1905.12322*, 2019.

[35] J. Kaplan, S. McCandlish, T. Henighan, T. B. Brown, B. Chess, R. Child, S. Gray, A. Radford, J. Wu, and D. Amodei, “Scaling Laws for Neural Language Models,” *arXiv preprint arXiv:2001.08361*, 2020.

[36] P. Micikevicius, S. Narang, J. Alben, G. Diamos, E. Elsen, D. Garcia, B. Ginsburg, M. Houston, O. Kuchaiev, G. Venkatesh, and H. Wu, “Mixed Precision Training,” *Int'l Conf. on Learning Representations (ICLR)*, 2018.

[37] P. Micikevicius, D. Stosic, N. Burgess, M. Cornea, P. Dubey, R. Grisen-thwaite, S. Ha, A. Heinecke, P. Judd, J. Kamalu, N. Mellemundi, S. Oberman, M. Shoeybi, M. Siu, and H. Wu, “FP8 Formats for Deep Learning,” *arXiv preprint arXiv:2209.05433*, 2022.

[38] M. Naumov, D. Mudigere, H.-J. M. Shi, J. Huang, N. Sundaraman, J. Park, X. Wang, U. Gupta, C.-J. Wu, A. G. Azzolini, D. Dzhulgakov, A. Mallevich, I. Cherniavskii, Y. Lu, R. Krishnamoorthi, A. Yu, V. Kondratenko, S. Pereira, X. Chen, W. Chen, V. Rao, B. Jia, L. Xiong, and M. Smelyanskiy, “Deep Learning Recommendation Model for Personalization and Recommendation Systems,” *arXiv preprint arXiv:1906.00091*, 2019.

[39] A. Nichol and P. Dhariwal, “Improved Denoising Diffusion Probabilistic Models,” *arXiv preprint arXiv:2102.09672*, 2021.

[40] NVIDIA. (2022) Using fp8 with transformer engine. [Online]. Available: https://docs.nvidia.com/deeplearning/transformer-engine/user-guide/examples/fp8_primer.html#Introduction-to-FP8

[41] V. Panayotov, G. Chen, D. Povey, and S. Khudanpur, “LibriSpeech: An ASR Corpus Based on Public Domain Audio Books,” *Int'l Conf. on Acoustics, Speech and Signal Processing (ICASSP)*, pp. 5206–5210, 2015.

[42] R. Pope, S. Douglas, A. Chowdhery, J. Devlin, J. Bradbury, A. Levskaya, J. Heek, K. Xiao, S. Agrawal, and J. Dean, “Efficiently scaling transformer inference,” *arXiv preprint arXiv:2211.05102*, 2022.

[43] S. Qian Zhang, B. McDanel, and H. T. Kung, “FAST: DNN Training Under Variable Precision Block Floating Point with Stochastic Rounding,” *International Symposium on High-Performance Computer Architecture (HPCA)*, pp. 846–860, 2022.

[44] S. Rajbhandari, C. Li, Z. Yao, M. Zhang, R. Y. Aminabadi, A. A. Awan, J. Rasley, and Y. He, “Deepspeed-moe: Advancing mixture-of-experts inference and training to power next-generation ai scale,” *arXiv preprint arXiv:2201.05596*, 2022.

[45] P. Rajpurkar, J. Zhang, K. Lopyrev, and P. Liang, “SQuAD: 100,000+ Questions for Machine Comprehension of Text,” *arXiv preprint arXiv:1606.05250*, 2016.

[46] M. Sandler, A. Howard, M. Zhu, A. Zhmoginov, and L.-C. Chen, “Mobilnetv2: Inverted Residuals and Linear Bottlenecks,” *Conf. on Computer Vision and Pattern Recognition (CVPR)*, pp. 4510–4520, 2018.

[47] S. Shen, Z. Dong, J. Ye, L. Ma, Z. Yao, A. Gholami, M. W. Mahoney, and K. Keutzer, “Q-bert: Hessian based ultra low precision quantization of bert,” in *Proceedings of the AAAI Conference on Artificial Intelligence*, vol. 34, no. 05, 2020, pp. 8815–8821.

[48] D. Stosic and P. Micikevicius, “Accelerating AI Training with NVIDIA TF32 Tensor Cores,” *Nvidia blog*, 2021, accessed Dec 2022. [Online]. Available: <https://developer.nvidia.com/blog/accelerating-ai-training-with-tf32-tensor-cores/>

[49] X. Sun, J. Choi, C.-Y. Chen, N. Wang, S. Venkataramani, V. V. Srinivasan, X. Cui, W. Zhang, and K. Gopalakrishnan, “Hybrid 8-bit Floating Point (HFP8) Training and Inference for Deep Neural Networks,” *Advances in Neural Information Processing Systems (NeurIPS)*, vol. 32, 2019.

[50] B. G. Tabachnick, L. S. Fidell, and J. B. Ullman, *Using multivariate statistics*. pearson Boston, MA, 2007, vol. 5.

[51] H. Touvron, M. Cord, M. Douze, F. Massa, A. Sablayrolles, and H. Jegou, “Training Data-Efficient Image Transformers & Distillation Through Attention,” *Int'l Conf. on Machine Learning (ICML)*, vol. 139, pp. 10 347–10 357, July 2021.

[52] A. Vaswani, N. Shazeer, N. Parmar, J. Uszkoreit, L. Jones, A. N. Gomez, Ł. Kaiser, and I. Polosukhin, “Attention is All You Need,” *Advances in Neural Information Processing Systems (NeurIPS)*, vol. 30, 2017.

[53] N. Wang, J. Choi, D. Brand, C.-Y. Chen, and K. Gopalakrishnan, “Training Deep Neural Networks with 8-bit Floating Point Numbers,” *Advances in Neural Information Processing Systems (NeurIPS)*, vol. 31, 2018.

[54] N. Weste and D. Harris, *CMOS VLSI Design: A Circuits and Systems Perspective*, 4th ed. USA: Addison-Wesley Publishing Company, 2010, p. 457.

[55] Y. Wu, M. Schuster, Z. Chen, Q. V. Le, M. Norouzi, W. Macherey, M. Krikun, Y. Cao, Q. Gao, K. Macherey, J. Klingner, A. Shah, M. Johnson, X. Liu, Łukasz Kaiser, S. Gouws, Y. Kato, T. Kudo, H. Kazawa, K. Stevens, G. Kurian, N. Patil, W. Wang, C. Young, J. Smith, J. Riesa, A. Rudnick, O. Vinyals, G. Corrado, M. Hughes, and J. Dean, “Google's Neural Machine Translation System: Bridging the Gap between Human and Machine Translation,” *arXiv preprint arXiv:1609.08144*, 2016.

[56] G. Xiao, J. Lin, M. Seznec, J. Demouth, and S. Han, “Smoothquant: Accurate and efficient post-training quantization for large language models,” *arXiv preprint arXiv:2211.10438*, 2022.

[57] B. Zhang, L. Luo, X. Liu, J. Li, Z. Chen, W. Zhang, X. Wei, Y. Hao, M. Tsang, W. Wang, Y. Liu, H. Li, Y. Badr, J. Park, J. Yang, D. Mudigere, and E. Wen, “DHEN: A Deep and Hierarchical Ensemble Network for Large-Scale Click-Through Rate Prediction,” *arXiv preprint arXiv:2203.11014*, 2022.